An Energy Scheduling Algorithm for New Energy Vehicles Based on Continuous-Time Differential Equation Modeling and Model Predictive Control

Xue Li*‡

*Xingtai Open University, Xingtai City, Hebei Province, 054000, China

‡Corresponding Author; Xue Li, li241129@126.com

Received: 06.02.2026 Accepted: 02.04.2026

Abstract- The core contradiction in energy scheduling for new energy vehicles arises from a mismatch between the high-dimensional nonlinear characteristics of the energy system under complex dynamic driving conditions and the dual requirements of computational efficiency and accuracy in real-time optimization scheduling. To address this issue, this paper presents an energy scheduling algorithm based on continuous-time differential equation modeling within a model predictive control framework. A continuous-time differential equation model incorporating battery SOC (State of Charge) dynamics, vehicle dynamics, and regenerative braking is established, and an MPC (Model Predictive Control) framework is embedded to construct a physically constrained finite-time optimal control problem. Efficient numerical discretization and solution strategies are employed to achieve real-time optimization. Simulation and hardware-in-the-loop testing show that under four typical operating conditions, the algorithm's energy consumption per 100 km is 15.2 to 21.5 kWh/100 km, lower than regular strategies, classic MPC, and DQN (Deep Q-Network). The SOC change rate is reduced to between 0.35% and 1.25%, meeting the millisecond-level real-time requirements of the onboard system. This method combines physical interpretability and engineering deployability, and has application value in intelligent electric vehicle energy management, V2G (Vehicle-to-Grid) scheduling, and personalized energy-saving driving systems.

Keywords. Differential equation optimization; energy dispatch algorithm; model predictive control; battery soc dynamic modeling; new energy vehicles.

Nomenclature

SOC State of Charge; MPC Model Predictive Control; V2G Vehicle-to-Grid; PHEV Plug-in Hybrid Electric Vehicle; BEV Battery Electric Vehicle; PMSM Permanent Magnet Synchronous Motor; OCP Optimal Control Problem; RK4 Fourth-order Runge-Kutta Method; IPOPT Interior Point OPTimizer; WLTC Worldwide Harmonized Light Vehicles Test Cycle; NEDC New European Driving Cycle; C Battery rated capacity [Ah]; I Battery current [A];T Temperature [°C]

1. Introduction

The global new energy vehicle industry has experienced rapid development. The industry shows an accelerated transformation from policy driven to market led [1]. As a core region for global new energy vehicle research, development, and application, China has established a complete industrial chain covering the whole vehicle, battery, motor, electronic control, and charging infrastructure. China continues to lead in market size, technology iteration, and industrial ecosystem [2], [3]. Under the guidance of the dual carbon strategic goal, the country has promoted the popularization and high-quality development of new energy vehicles through policy combinations including dual-credit management, purchase incentives, and ease of use [4]. As consumers increasingly prioritize range safety performance and usage cost, the importance of vehicle energy efficiency management continues to grow[5]. In this context, the energy scheduling algorithm serves as the core control logic of the new energy vehicle energy management system [6],[7]. It directly determines the power distribution strategy between power sources, affects the vehicle's range and energy consumption performance, and relates to the charging and discharging safety, service life of the power battery, and the stability of whole vehicle operation. It has become a key technical link

restricting the improvement of the overall competitiveness of the product.

Under dynamic driving conditions, the energy system of new energy vehicles exhibits significantly high-dimensional nonlinear characteristics. The SOC open-circuit voltage curve of the power battery shows strong nonlinearity, the efficiency MAP of the drive motor has multiple extreme points, and the time-varying constraints of the braking energy recovery system pose a triple core contradiction to traditional scheduling strategies [8], [9]. These millisecond-level real-time control requirements mean that the algorithm should have ultra-high computational efficiency. The complex energy flow coupling relationship often leads traditional optimization methods into the dimensionality curse [10]. It is difficult to optimize the objectives of energy efficiency improvement and battery safety in a coordinated way during dynamic processes [11]. A crucial contradiction exists among control accuracy losses caused by simplifying models and the requirements for system robustness [12]. These problems together constitute the technical challenges to be overcome in new energy vehicle energy scheduling and highlight the theoretical research and engineering application value of the continuous-time differential equation modeling method [13]. When frequent acceleration or deceleration happens under complex road conditions, the traditional discrete-time model becomes difficult to characterize the dynamics precisely. This situation further aggravates contradictions between accuracy and real-time performance.

Existing energy scheduling methods for new energy vehicles mainly evolve along the technical path of "rule-based - data-driven - model optimization", but each has its insurmountable limitations. Rule-based strategies achieve power allocation by setting equivalent factors based on experience. These strategies are computationally efficient and simple to deploy in engineering applications, leading to their widespread use in large-scale hybrid systems. However, they rely heavily on prior knowledge of operating conditions. In non-standard or dynamically changing scenarios, the parameters cannot be adaptively adjusted, resulting in SOC deviation from the target and high energy efficiency loss [14], [15]. Data-driven approaches use neural networks to learn scheduling strategies from large simulation datasets. These techniques show major dynamic adaptability and are used to optimize the energy consumption under different operating conditions, including an NEDC (New European Driving Cycle). These methods lack explicit constraints derived from physical laws. Under extreme operating conditions, they are prone to output overcharging and over-discharging commands, resulting in simulation-real-domain offset problems and a significant decrease in generalization ability to actual roads [16], [17]. Model optimization methods plan balancing theoretical rigor with practical effectiveness. DP (Dynamic Programming) may give an opportunity to access a global best solution, although its computational complexity increases exponentially and does not satisfy requirements for real-time control [18]. PMP (Pontryagin's Minimum Principle) has high computational efficiency, but it relies too much on the information of the entire working condition, and its performance degrades sharply in unknown road conditions [19]. MPC adopts a rolling optimization mechanism and has a certain robustness, but it often linearizes or simplifies the structure of subsystems such as batteries and motors, resulting in model mismatch and large deviations in measured energy consumption [20]. The three types of methods are respectively caught in the contradiction of "experience dependence and working condition diversity", "dynamic adaptation and physical safety", and "theoretical optimality and engineering real-time", making it difficult to achieve high-precision modeling, strong safety constraints, and low-latency solutions in complex driving scenarios. This forms a long-term "precision-efficiency-safety" triangular bottleneck that restricts the improvement of energy scheduling performance, and a new paradigm that integrates continuous physical models and efficient online optimization is urgently needed to break through this bottleneck.

To address the challenges mentioned earlier, this research applies a novel energy scheduling algorithm for new energy vehicles based on high-fidelity continuous-time differential equation modeling. At first, a continuous-time coupled model using differential equations is constructed by integrating battery SOC dynamics, vehicle dynamics, and regenerative braking mechanisms. This approach enhances the physical consistency within the system description and can avoid accuracy loss when sudden changes in the operating conditions occur because of discrete modeling. An MPC framework integrating this differential model is designed, employing numerical discretization methods that balance accuracy and computational efficiency, to meet the 100 ms real-time need of the vehicle system.

Simulation experiments show that under different operating conditions, including WLTC (Worldwide Harmonized Light Vehicles Test Cycle), NEDC, and high-speed cruising, the algorithm performs well, with a much-reduced standard deviation in fluctuation of motor power compared to those from baseline methods. This paper solves the problem of "accuracy-efficiency-safety" co-optimization of battery electric vehicle energy scheduling and proposes a new approach combining theoretical innovation with engineering practicality.

2. Modeling of Energy Systems for New Energy Vehicles

2.1. System Architecture and Energy Flow Analysis

The architectural design of the energy dispatch system of new energy vehicles directly determines the energy conversion efficiency and the complexity of optimization control. This design requires targeted analysis based on differences in power system topology. This study focuses on battery electric vehicles, in which the power battery serves as the sole energy source and the permanent magnet synchronous motor functions as the sole propulsion actuator. The vehicle under study is a pure battery electric vehicle with no internal combustion engine. The energy scheduling algorithm determines the motor output power and the regenerative braking intensity coefficient. The driver’s speed demand is treated as a prescribed reference trajectory, and the controller optimizes the power allocation under this fixed driving cycle. There are major differences in energy flow characteristics.

2.1.1. Comparison of power platform topology

This architecture makes up many links for an energy conversion, so the overall system efficiency is usually lower compared to a parallel architecture. However, it provides decoupling control between the engine and wheels. It also simplifies the strategy for distributing power.

2.1.2. Core component technical parameter system

The boundary conditions of the energy scheduling algorithm are required to be constructed on the basis of physical characteristic parameters from the major components, which primarily include these major elements.

Power battery system [21]: The energy density for a ternary lithium battery used in mainstream vehicle models is 200-300 Wh/kg. Meanwhile, the density found in lithium iron phosphate batteries achieves 100-200 Wh/kg.

Drive motor [22]: PMSMs (Permanent Magnet Synchronous Motors) occupy the mainstream market share. Traditional motors have a peak power density that is between 3 and 5 kW per kg. The peak efficiency presents values from 95% up to 97%. There is a speed range limited to approximately 4,000 rpm, even as high as 15,000 rpm.

Braking system [23]: The brake-by-wire system, in conjunction with the ESP hev (Electronic Stability Program Hybrid Electric Vehicle) module, can achieve regenerative braking energy recovery in the maximum deceleration range of 0.3 g. The recovery efficiency is affected by both the motor's reverse drag characteristics and the battery's SOC state.

Forward energy transfer path: DC electrical output produced by a power battery provides three-phase AC electricity after conversion through inverter devices, which are used to drive the motor efficiently. The motor then transmits torque to the wheels through the reduction gear, together with the differential mechanism. It must be noted that losses exist during each conversion stage; for example, inverter efficiency generally ranges between about 95%-98%, but permanent magnet motor efficiency depends on load rate, with possible variation from nearly only 85% until the highest at around even just near to 97%.

Reverse energy transfer path: The wheels reverse-drive the motor through the mechanical transmission system to enter the generator state. The three-phase AC power is rectified into DC power by the inverter, and then transmitted through a DC/DC converter. The Direct Current converter will charge the battery when matched under an appropriate voltage for this purpose.

Key constraints make up motor generation efficiency rates, capacities of battery charging acceptance levels, and also coordinated management of braking intensity control.

2.2. Modeling of Continuous-Time Differential Equations

This study focuses on constructing three types of key differential equation models covering variable definitions, parameter characteristics, and derivation processes. These models form a complete system dynamic description framework.

The SOC dynamic model is constructed on the ampere-hour integral technique [24]. It is derived from the battery rated capacity C (unit Ah) and calculates the SOC change rate by real-time monitoring of the charging and discharging current I (unit A). The core differential equation is expressed as:

$$\frac{d(\mathrm{SOC})}{dt} = -\frac{I}{3600C}\cdot\eta_{\mathrm{coulomb}}(T,I) \tag{1}$$

In equation (1), 3600 is the time conversion coefficient (seconds to hours), and the negative sign indicates that the SOC decreases during discharge. SOC is the state of charge, t is time in seconds, I is the battery current in amperes with positive values for discharge, C is the battery rated capacity in ampere-hours, and $\eta_{\mathrm{coulomb}}(T,I)$ is the coulombic efficiency as a function of temperature T in degrees Celsius and current I. To enhance the accuracy of the model, a coulomb efficiency correction term $\eta_{\mathrm{coulomb}}(T,I)$ related to temperature T and current I is employed, and this coefficient takes a value between zero and one.

The longitudinal dynamic equations of the vehicle are derived from Newton's second law [25], and the expression is:

$$\begin{aligned} F_{\mathrm{air}} &= 0.5\rho C_d S_{area}\, v^2 \\ F_{\mathrm{roll}} &= mgf\cos\theta \\ F_{\mathrm{grade}} &= mg\sin\theta \\ m\frac{dv}{dt} &= F_{\mathrm{tractive}} - F_{\mathrm{air}} - F_{\mathrm{roll}} - F_{\mathrm{grade}} \end{aligned} \tag{2}$$

In equation (2), $\frac{dv}{dt}$ corresponds to acceleration expressed in m/s², while m denotes vehicle mass measured in kg. ρ is the air density in kg/m³, C_d is the drag coefficient, S_{area} is the frontal area in m², v is vehicle speed in m/s, m is vehicle mass in kg, g is gravitational acceleration in m/s², f is the rolling resistance coefficient, θ is the road grade angle in radians, and F_{tractive} is the tractive force in newtons. The four terms appearing on the right side of this equation represent a dynamic equilibrium, which is between the driving force F_{tractive} and three categories of driving resistances. Aerodynamic resistance F_{air} gets determined by using an empirical formula $0.5\rho C_d S_{area}\, v^2$, where C_d refers to the drag coefficient, ρ means air density, S_{area} gives the frontal area used in m², and v is velocity for a vehicle given as m/s; rolling resistance F_{roll} can be described through $mgf\cos\theta$ where f signifies the rolling resistance coefficient and θ indicate road gradient angle; lastly, a gradient resistance F_{grade} formulates as $mgsin\theta$. Here θ is assigned positive values during uphill movement but negative ones during downhill movement.

The regenerative braking model is constructed using a front-to-rear axle braking force distribution strategy [26]. The core of this model is to establish a dynamic relationship between regenerative braking force F_{regen} and brake pedal travel. When the operator pushes the brake pedal, the system estimates the total braking force requirement based on a pedal travel signal. According to a "front axle primary braking"

principle that is necessary by the ECE R13 braking regulations [27], 60%-70% of braking force goes to the front axle. Subject to the condition that the braking safety requirements are being satisfied, regenerative braking through a motor is given priority. When the demand for braking force at the front axle is lower than the maximum capacity of regenerative braking from the motor, F_{regen} becomes equal to the front axle braking force. Any demand that goes above such capacity has to be compensated for by mechanical braking.

The recovered energy E_{regen} is calculated using an integral equation, as shown in the following equation:

$$E_{\text{regen}}=\int F_{\text{regen}}\cdot v\,dt\cdot\eta_{\text{motor}} \tag{3}$$

In equation (3), η_{motor} signifies the regenerative efficiency of the motor-inverter system, and v denotes the instantaneous vehicle speed during braking.

The three forms of differential equations are coupled dynamically via variables such as current I and vehicle speed v. If the vehicle accelerates, F_{tractive} becomes higher, making I increase, which then influences battery state through the SOC model. When there is braking action, F_{regen} gives a negative current that corrects the rate of change for SOC in an inverse way.

2.3. Nonlinear Characteristics and Constraints of the Model

The nonlinear characteristics of the energy dispatch model for new energy vehicles stem from the complex physical behavior of the coulombic efficiency in the battery system, the motor efficiency in the drive system, and the regenerative braking efficiency in the braking energy recovery system, as shown in Fig. 1.

The coulombic efficiency η_{coulomb} in the battery system exhibits significant multivariate nonlinear characteristics, as shown in Fig. 1(a) for nonlinear surface fitting. Nonlinearity inside the drive system is reflected mostly within surface distribution characteristics relating to PMSM efficiency MAP. The nonlinearity for the regenerative braking system has a strong coupling relation with the efficiency of the vehicle during regenerative brake operation.

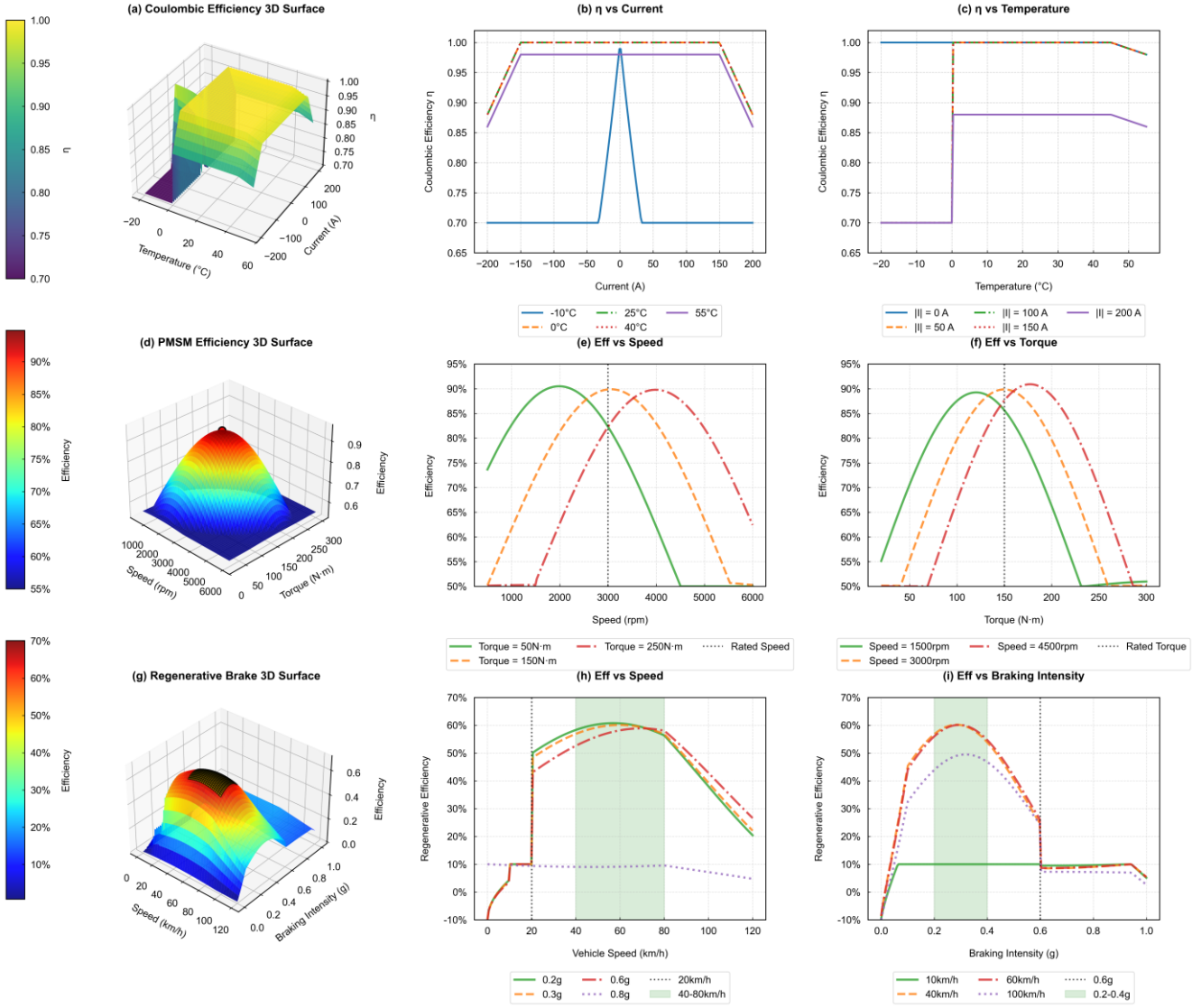

Fig. 1. Characteristics of three types of nonlinear surfaces

The coulomb efficiency value is dynamically adjusted with the change of operating temperature and charge/discharge current [28]. Fig. 1(b) shows that when the temperature is below 0℃, $\eta_{coulomb}$ decreases exponentially with the rise of the absolute value of the current, and losses occur when discharging at a high rate >150A; Fig. 1(c) shows that the coulomb efficiency curve tends to be flat in the ideal range of 25℃~40℃.

PMSM under different speed-torque combinations is shown as a non-convex three-dimensional surface in Fig. 1(d). It forms an efficiency peak region near the rated operating conditions (Fig. 1(e) speed 3000 rpm, Fig. 1(f) torque 150 N·m), and its efficiency drops significantly in the low-speed, high-torque or high-speed, low-torque regions. Traditional linear optimization approaches have difficulty in capturing the global optimum precisely. This gives an opportunity to use nonlinear programming techniques for dealing with multi-extremum problems.

Fig. 1(g) demonstrates that the efficiency of regenerative braking is affected by the velocity of the vehicle and the magnitude of the applied braking force. When the vehicle speed is below 20 km/h (Fig. 1(h)) or the braking intensity exceeds 0.6g (Fig. 1(i)), the mechanical braking intervention ratio increases significantly, causing the regenerative efficiency to drop sharply to below 20%. At low to medium speed, between 40-80 km/h, and with medium braking intensity between 0.2-0.4g, the regenerative efficiency can remain relatively high at a value of 50 % to 60 %.

To ensure balance between system safety and performance, the model must obey the boundaries of these physical constraints very strictly.

The SOC safety window is restricted to a range of [0.2, 0.9]. A value less than 0.2 can lead to an over-discharge damage of the battery, while a value higher than 0.9 gives an opportunity for an increased risk of thermal runaway.

The battery charge/discharge power limit P_{batt_max} is a binary function of SOC and temperature:

$$P_{batt}(t) \le P_{batt\_max}(SOC,T) \begin{cases} P_{batt\_max}(0.5,25^{\circ}C)=200kW \\ P_{batt\_max}(SOC \le 0.2, T \le -10^{\circ}C) \le 80kW \end{cases} \quad (4)$$

In equation (4), P_{batt_max} has a maximum discharge power of 200kW at 25℃ and SOC=0.5. When SOC drops to 0.2 or the temperature is below -10℃, this limit drops sharply to below 80kW.

The motor output torque limit T_{motor_max} has a piecewise linear relationship with the speed.

$$T_{motor}(t) \le T_{motor\_max}(\omega) = \begin{cases} T_{max}, & \&\&\omega \le \omega_{base}(\omega_{base}=2000\sim3000rpm) \\ T_{max} \cdot \dfrac{\omega_{base}}{\omega}, & \&\&\omega > \omega_{base} \end{cases} \quad (5)$$

In equation (5), the maximum torque output remains constant below the T_{motor_max} base speed (usually 2000~3000rpm), and decreases inversely with the increase of speed after exceeding the base speed.

In addition, the braking system is equipped with a hard constraint on the maximum regenerative power $P_{regen}(t) \le P_{regen\_max}$=80 kW to prevent excessive recharge current from impacting the battery management system.

Multi-physics coupling leads to a highly sparse Jacobian matrix in the system, making it easy for traditional gradient descent methods to get trapped in local optima; the time-varying nature of the constraints requires the algorithm to have online adaptive adjustment capabilities; the non-convexity of the efficiency surface causes the objective function to exhibit a multi-peak distribution, requiring the combination of global optimization strategies to improve the solution quality.

In the differential equation model constructed in this study, the mapping relationships between the variables—temperature, current, rotational speed, torque, vehicle speed, and braking intensity—and the corresponding efficiencies, along with the key threshold values, are defined as the core parameters characterizing the system nonlinearity. The values are a combination of existing research conclusions and engineering practice experience.

3. Design of Energy Scheduling Algorithm Based on Continuous-Time Differential Equation Modeling

3.1. Problem Formalization: Construction of the OCP (Optimal Control Problem)

The energy dispatching problem for battery electric vehicles is formalized as a dynamic optimization problem governed by continuous-time differential equations. Unlike the linear battery model or simplified vehicle dynamics model typically used in classic MPC strategies, the OCP constructed in this paper is directly based on the previously established continuous-time nonlinear differential equation coupled model. By defining state variables, control variables, objective functions, and constraints, a complete optimal control model framework is established to achieve efficient energy allocation during vehicle operation and meet the state maintenance requirements of the power battery.

Based on the dynamic properties of the energy system of new energy vehicles, the state vector equation is defined as follows:

$$x = \begin{bmatrix} SOC \\ v \end{bmatrix} \quad (6)$$

In equation (6), the state vector x contains the battery state of charge SOC and the vehicle speed v in m/s. Equation (6) contains two core state variables: SOC and vehicle speed v. SOC signifies the present energy storage capacity of the battery and affects the driving range and battery health. Vehicle speed v is among the major parameters that describe the dynamic behavior of a vehicle, as well as defines the demand for an instantaneous power.

The control vector is designed as follows:

$$u = \begin{bmatrix} P_{motor} \\ \beta_{regen} \end{bmatrix} \quad (7)$$

In equation (7), the control vector u contains the motor output power P_{motor} in kilowatts and the regenerative braking intensity coefficient β_{regen} which ranges from 0 to 1. P_{motor} is

the output power of the drive motor, and the positive value means driving, whereas the negative value represents braking. β_{regen} is the regenerative braking intensity coefficient. It receives a value in a range from zero to one and adjusts the proportion of energy recovery during braking. The control authority of the energy scheduling system is limited to the motor output power P_{motor}, which directly determines the traction or braking torque applied to the wheels, and the regenerative braking intensity coefficient β_{regen}, which governs the proportion of braking energy recovered. The driver's speed demand is treated as a prescribed reference trajectory, and the controller optimizes the power allocation under this fixed driving cycle.

$$J = \int_{t_0}^{t_f} [\lambda_1 P_{\text{loss}}(t) + \lambda_2 (SOC(t) - SOC_{\text{ref}}(t))^2]\, dt \tag{8}$$

The objective function utilizes an integral performance index, and its expression is:

In equation (8), J is the cost functional, t_0 and t_f are the start and end times in seconds, $P_{\text{loss}}(t)$ is the total system power loss in kilowatts, $SOC_{\text{ref}}(t)$ is the reference state of charge trajectory, and λ_1 and λ_2 are positive weighting coefficients. the integral interval $[t_0, t_f]$ stands for the time range of a single driving task. Two important optimal objectives are integrated into the objective function by linear weighting: the total system energy consumption P_{loss}, and the SOC rate of change. P_{loss} denotes the sum of the energy losses of the drive system, where the relevant losses are motor losses and battery internal resistance losses. Motor losses mainly consist of copper losses, iron losses, and mechanical losses. Magnitude of these is decided by output power, speed, as well as the efficiency characteristics. Battery internal resistance losses are proportional to the square value of the current that passes through the battery multiplied by the internal resistance. These can be represented with I^2R formula, where I indicates charging or discharging current and R is equivalent to the internal resistance of the battery. λ_1 and λ_2 refer to the energy consumption weighting coefficient and the SOC tracking weighting coefficient, respectively, and they balance the optimization objectives between energy efficiency and SOC maintenance precision.

Therefore, values for λ_1 and λ_2 need periodic updating according to the driving scenario, together with the control objective. During long-distance driving, λ_1 can be increased to optimize the reduction in energy consumption, while during short-distance urban driving conditions, λ_2 can be increased to improve the accuracy in SOC tracking. In practical applications, the coefficient values are determined by combining offline optimization with online adaptive adjustment. By using generic driving condition datasets, initial coefficients are calculated offline via a genetic algorithm or particle swarm optimization technique. During real-time control, the weight coefficients are dynamically adjusted according to the current SOC deviation and energy consumption level to achieve an adaptive balance of the optimization objective.

The dynamic constraints of the system are described by differential equations of the state variables, namely:

$$\frac{dx}{dt} = f(x,u,t) \tag{9}$$

Equation (9) represents the system dynamics, where f(x,u,t) is the vector-valued function containing the differential equations for SOC and vehicle speed. Equation (9) includes the SOC dynamic equation and the vehicle speed dynamic equation. The SOC dynamic equation comes from the relation between the battery charge/discharge current and the capacity. It shows the rate at which SOC changes over time. The vehicle speed dynamic equation follows the principle of balance in vehicle dynamics; it explains relationships among the driving force, braking force, driving resistance, and acceleration. Regenerative braking intensity β_{regen} indirectly affects vehicle speed change by influencing braking torque distribution. The boundary conditions are set as follows:

$$\mathbf{x}(t_0) = \mathbf{x}_0, \mathbf{x}(t_f) = \mathbf{x}_f \tag{10}$$

In equation (10), $\mathbf{x}_0$ is the initial state vector at time t_0, and $\mathbf{x}_f$ is the terminal state vector at time t_f. the initial state $\mathbf{x}_0 = \begin{bmatrix} \text{SOC}_0 \\ v_0 \end{bmatrix}$ is determined by the actual SOC and initial vehicle speed at the start of the driving task; the terminal state $\mathbf{x}_f = \begin{bmatrix} \text{SOC}_f \\ v_f \end{bmatrix}$, v_f is usually 0 (corresponding to the finishing of the driving task), and SOC_f is a preset terminal SOC constraint value, which is used to ensure that the battery state meets the subsequent usage requirements when the driving ends.

3.2. MPC Framework Design

The selection of the control time domain N_c and the prediction time domain N_p needs to balance the system's dynamic response and computational complexity. Derived from distinctions existing in vehicle operating conditions, a prediction time domain of 10 seconds is employed for the urban environments, and it is extended to 15 seconds during high-speed conditions. The control time domain is set at 1/3 of the prediction time domain, i.e., N_c=3.33 seconds for urban conditions and N_c=5 seconds for high-speed conditions.

The MPC framework adopts a closed-loop iterative mechanism of prediction-optimization-feedback, as shown in Fig. 2.

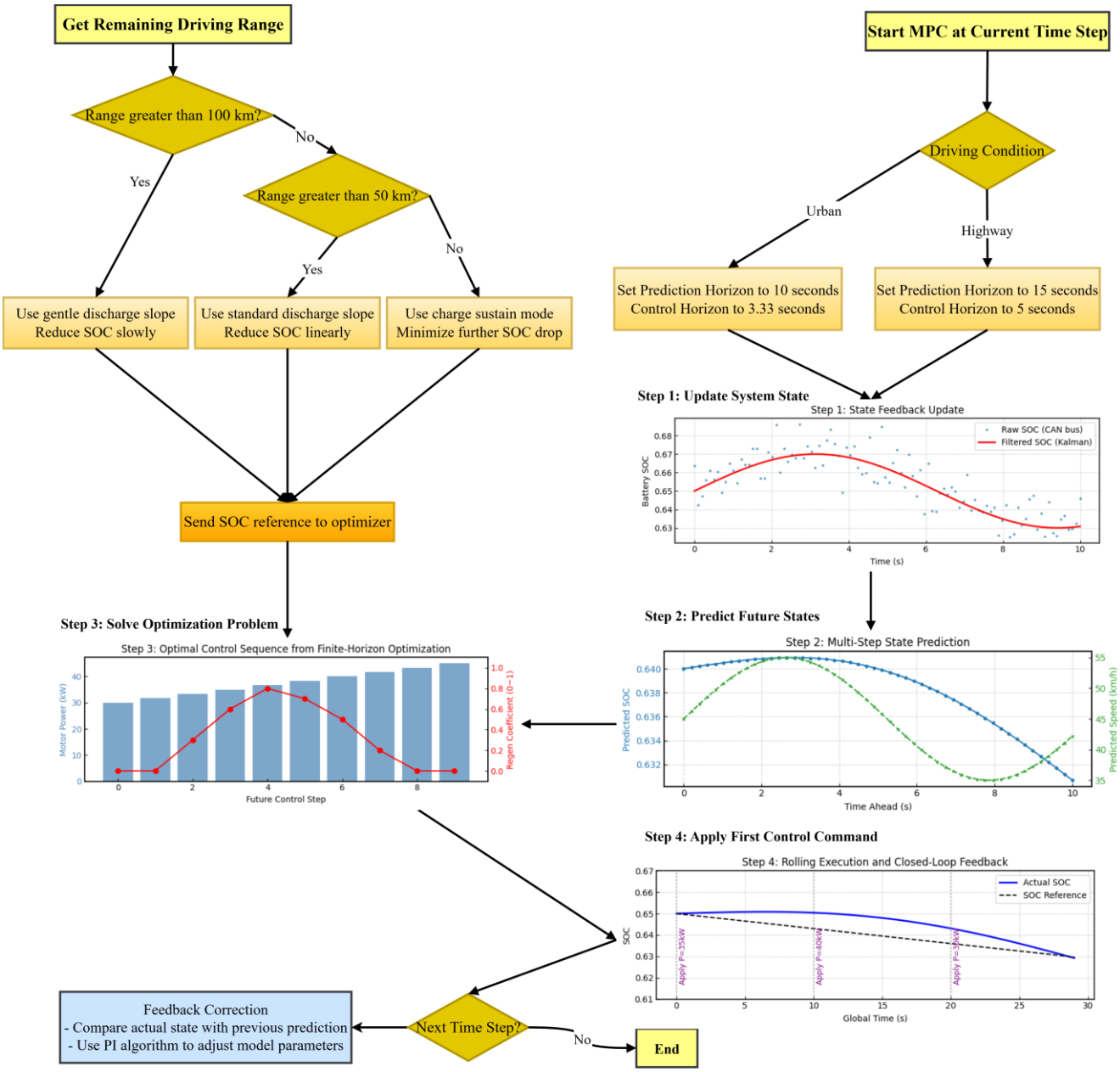

Fig. 2. MPC framework

Fig. 2 depicts the comprehensive operational workflow of MPC in the energy dispatching of new energy vehicles. The system collects noisy raw SOC state data with the sensors, giving an opportunity to access smoother and more reliable estimation by using Kalman filtering for current state calculation. Based on a differential equation model, it performs multi-step predictions of the battery SOC and vehicle velocity for the next ten seconds. On this basis, it solves a constrained finite-time optimization problem to generate a future control sequence, including motor power and regenerative braking intensity. Only the first step of the sequence is executed, and this process is repeated in subsequent cycles to form a closed-loop feedback, achieving accurate SOC tracking of the reference trajectory and efficient energy utilization. The detailed procedures are outlined below:

(1) Status feedback update: The current vector representing the vehicle status $x(k)$ is collected via CAN (Controller Area Network) bus, which includes major parameters like battery SOC, motor output power, and speed of the vehicle. Kalman filtering is applied to remove sensor noise interference.

(2) Multi-step state prediction: Based on the established differential equation model (including the battery equivalent circuit model and the power system efficiency model), the future state sequence $\mathbf{x}(k|k) = \mathbf{x}(k + N_p|k)$ is generated in the prediction time domain N_p. The battery SOC prediction adopts the improved Thevenin [29] equivalent circuit model.

(3) Finite Time Domain Optimization: With energy consumption minimization and SOC maintenance as the dual objective functions, a quadratic programming problem with inequality constraints on motor power limiting and battery charging and discharging current limiting is constructed, and

the optimal control sequence $\mathbf{u}(k|k) = \mathbf{u}(k + N_c - 1|k)$ in the control time domain is obtained by solving it.

(4) Rolling time domain execution: The initial control quantity $u(k|k)$ is used as an actuator to modify the motor operating mode. The aforementioned procedure is reiterated at each subsequent sampling interval to form a rolling optimization closed loop.

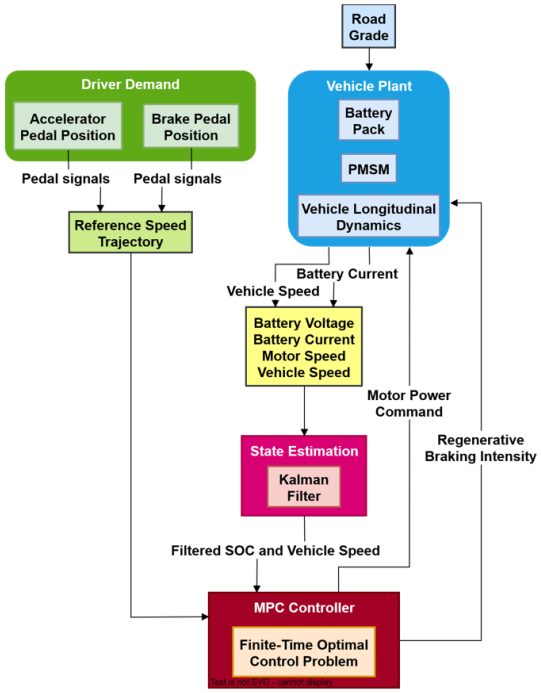

Fig. 3. Block diagram of the proposed energy scheduling control strategy

Fig. 3 comprises four main modules. The Driver Demand module inputs the accelerator pedal position and brake pedal position, generating the reference vehicle speed trajectory. The State Estimation module receives raw sensor data including battery voltage, battery current, motor speed, and vehicle speed, and outputs the filtered SOC and vehicle speed using a Kalman filter. The MPC Controller module takes the reference speed trajectory and estimated states, solves the finite-time optimal control problem based on the continuous-time differential equation model, and outputs the optimal motor power command and regenerative braking intensity coefficient. The Vehicle Plant module includes the battery pack, permanent magnet synchronous motor, and vehicle longitudinal dynamics. The motor power command is sent to the motor driver, and the regenerative braking coefficient controls the brake-by-wire system. Feedback loops connect the vehicle speed and battery current back to the State Estimation module. A disturbance input from road grade is also fed into the Vehicle Plant module.

The SOC reference trajectory SOC_{ref} is constructed using a piecewise linear programming method, and the slope is dynamically adjusted based on the remaining mileage.

$$SOC_{ref}(s)=\begin{cases} SOC_0-0.0005\cdot s, & \&\&s>100\text{km} \\ SOC_{100}-0.001\cdot(s-100), & \&\&50\text{km}<s\leq 100\text{km} \\ SOC_{50}-0.0002\cdot(s-50), & \&\&s\leq 50\text{km} \end{cases} \quad (11)$$

In equation (11), when the remaining mileage is >100km, a gradual descent strategy is adopted with a slope of -0.0005 /km; in the 50-100km range, a linear descent is switched with a slope of -0.001 / km; at 50km, the ≤power preservation mode is entered with a slope of -0.0002 / km.

To address the model mismatch problem, the framework applies a feedback correction mechanism, which uses the deviation Δx between the predicted state $x(k|k-1)$ and the current actual state $x(k)$ to correct the prediction model parameters in real time using the PI (Proportional Integral) correction algorithm [30].

3.3. Efficient Numerical Implementation Strategy

This study constructs an efficient numerical implementation strategy from four dimensions: discretization method selection, nonlinear optimization transformation, solver configuration, and computational acceleration, and compares it with the real-time requirements of energy scheduling algorithms for new energy vehicles.

(1) Accuracy-efficiency balance of discretization methods

In the discretization stage of dynamic systems, the implicit Euler method [31],[32] is selected due to its unconditional numerical stability and lower per-step computational cost. Considering that the dynamics of the system described by high-fidelity differential equations are more complex, and the computational resources of the vehicle-mounted embedded system are limited, the implicit Euler method, which achieves the best balance between accuracy and efficiency, is finally selected as the discretization tool to ensure the stability and speed of the optimization loop. The final implementation adopts the implicit Euler method for discretization.

(2) Transformation techniques for nonlinear optimization problems

To address the strong nonlinearity present in high-fidelity models, a continuous approximation of the motor efficiency map is constructed using cubic spline interpolation over the torque-speed plane. The interpolation preserves the nonlinear efficiency characteristics across the full operating range while maintaining differentiability. The transformed model contains 1200 nonlinear equality constraints derived from the spline interpolation and is formulated as a continuous nonlinear programming problem. No binary or integer variables are introduced in this formulation. The optimization problem remains a continuous nonlinear program. Simultaneously, the CasaADi automatic differentiation toolkit is used to perform gradient analysis on the objective function's energy minimization and state constraints, generating sparse representations of the Jacobian and Hessian matrices.

(3) Configuration of IPOPT (Interior Point OPTimizer) solver according to an interior point approach

IPOPT is selected as the solver for the resulting continuous nonlinear program, as it efficiently handles large-scale sparse problems with nonlinear constraints. The problem contains no integer decision variables, therefore IPOPT is directly applicable.

The maximal number of iterations has been set at 50 to balance between solution accuracy and computational time. The convergence tolerance is set to a certain value 10^{-4}. The MUMPS (Multi-frontal Massively Parallel Solver) is chosen as the linear solver. Since the optimization problem is formulated as a continuous nonlinear program without integer variables, IPOPT is directly applicable.

(4) Multi-level computing acceleration technology

A strategy with two stages for acceleration is applied, which helps to minimize solution time. Warm-start initialization gives the opportunity to access the previous optimal solution from the last time step as an initial value for the current problem, which improves the speed of iteration convergence. A warm-start initialization strategy reuses the optimal solution from the previous time step as the initial guess for the current problem, accelerating iteration convergence. The numerical implementation is executed on the embedded multi-core processor of the dSPACE SCALEXIO hardware-in-the-loop platform. All computations are performed on the CPU without GPU acceleration, ensuring the reported timing results reflect realistic in-vehicle computational constraints.

4. Simulation Experiments and Result Analysis

4.1. Experimental Setup

4.1.1. Simulation platform and test conditions

MATLAB/Simulink 2023a serves as the core modeling tool. The CarSim 2022.1 vehicle dynamics module is integrated through the S-Function interface to achieve joint simulation of the energy system and vehicle physical characteristics. No real-vehicle data collection or real-road testing was performed in this study. All evaluations are based on numerical simulation and hardware-in-the-loop emulation.

The CarSim module includes a PAC2002 tire model with a longitudinal stiffness of 280 N/mm and a lateral stiffness of 180 N/deg, as well as a brake-by-wire system model, reproducing vehicle dynamics under different road surface adhesion coefficients. The simulation environment uses an Intel i7-12700K processor (12 cores, 20 threads, maximum turbo frequency 5.0GHz) and 32GB of DDR4-3200 memory for offline model development and parameter calibration. Real-time performance evaluation is conducted on the dSPACE SCALEXIO hardware-in-the-loop platform, which contains an embedded multi-core processor (Infineon AURIX TC397) with a clock frequency of 300 MHz, representing the computational capability of mainstream automotive domain controllers. All computations are performed on the embedded CPU without GPU acceleration. The control cycle is set to 100 milliseconds. When the optimization solver exceeds this cycle, the system holds the previous control action unchanged until the next successful solve.

To assess the practical computational efficiency of the algorithms in an in-vehicle environment, all comparison algorithms were deployed to the dSPACE SCALEXIO hardware-in-the-loop platform for testing. This platform includes an embedded multi-core processor with computing capability comparable to mainstream automotive domain controllers. It can reliably show the real-time functioning of used algorithms.

Four typical driving cycles were selected to cover the energy characteristic test in all scenarios, from standard regulations to actual roads. Fig. 4 depicts the test speed and the driving distance associated with the driving cycle.

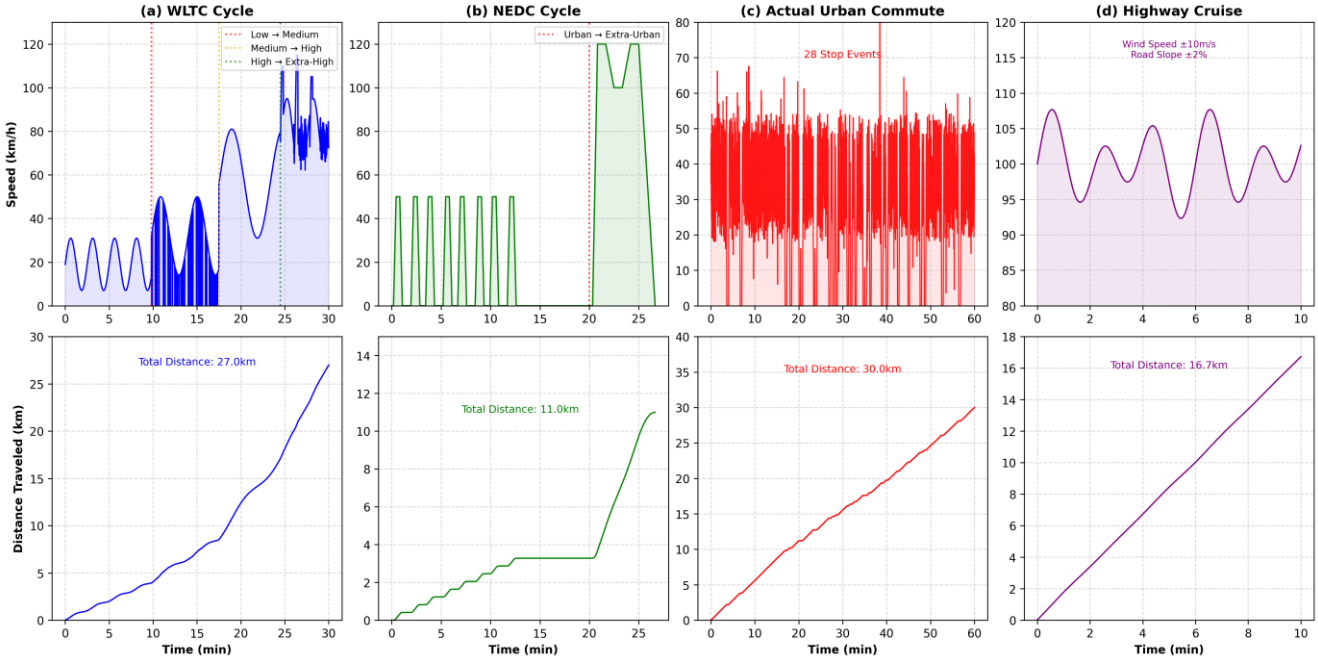

Fig. 4. Typical driving cycle conditions

(1) WLTC operating condition.

Low-speed section: 4 km, average speed 19 km/h; Medium-speed section: 7 km, average speed 32 km/h; High-

speed section: 11 km, average speed 56 km/h; Ultra-high-speed section: 5 km, average speed 75 km/h. Total driving distance: 27 km, total time: 1800 s. The speed-time curve in Fig. 4(a) shows a periodic fluctuation characteristic of acceleration-constant speed-deceleration, and the ultra-high-speed section includes 3 consecutive overtaking acceleration processes.

(2) NEDC cycle

The NEDC cycle covers a duration of 1600 seconds to traverse a total distance equal to 11.0 kilometers. This includes urban cycle running from 0 to 1200 seconds with four repeating segments where top speed reaches up to 50 km/h, and also a suburban cycle continuing between 1200 and 1600 seconds at the highest speed of about 120 km/h. The speed-time curve in Fig. 4(b) is smoother than that of the WLTC, and the suburban phase includes the full-throttle acceleration process from 0 to 120 km/h, reflecting the ideal driving mode.

(3) Actual urban commuting cycle

This data was collected during the morning rush hour on main roads in a first-tier city, with an average speed of 30.0 km/h and including 28 stop events. 90% of the vehicle speeds were distributed in the range of [0.0, 50.7] km/h, with the maximum single deceleration intensity being 1.2 m/s². Fig. 4(c) shows the frequent start-stop characteristics under congested conditions, with dense speed fluctuations and dispersed idling periods, closely resembling real-world urban driving scenarios.

(4) High-speed cruise cycle

This evaluation is designed for stable high-speed driving conditions. Cycle lasts for a period of 600 seconds while keeping base velocity around 100 km/h, giving an average actual speed of approximately 100.4 km/h. The velocity of the vehicle variation ranges from nearly 92.3 km/h up until the maximum recorded value at about 107.7 km/h, all being influenced by alternating tailwinds or headwinds (10 m/s) as well as gradients (+/-2%). Fig. 4(d) shows an approximately linear time-distance trajectory, indicating stable driving performance despite minor external disturbances.

4.1.2. Vehicle model parameters

Vehicle models that have been employed in simulation feature core parameters based on typical technical criteria among the mainstream of C-class pure electric sedans found currently on the market. The parameter settings are illustrated in Table 1.

Table 1. Test vehicle system parameters

Component	Parameter	Value
Vehicle	Class	Mid-size (C-segment) Battery Electric Vehicle (BEV)
	Curb Mass	2100 kg
	Wheelbase	2900 mm
	Front Track Width	1620 mm
	Drag Coefficient	0.28
	Rolling Resistance Coefficient	0.018
Traction Battery	Chemistry	NCM811
	Nominal Capacity	100 kWh
	Nominal Voltage	355 V
	Gravimetric Energy Density	280 Wh/kg
	Operating Temperature Range	–20 °C to 55 °C
Drive Motor	Type	PMSM
	Peak Power	180 kW
	Rated Power	90 kW
	High-Efficiency Zone (≥94%)	2000–8000 rpm

Note: The vehicle is equipped with a single permanent magnet synchronous motor as the sole propulsion source; no internal combustion engine is present.

Table 1 shows technical specifications for the experimental vehicle. The vehicle has been equipped with a 100 kWh NCM811 ternary lithium pile system, which features a nominal voltage of 355 V, a gravimetric energy density of 280 Wh/kg, and a functional temperature range that ranges from -20°C to 55°C. The propulsion system uses a permanent magnet synchronous motor where maximum and rated power outputs are set as 180 kW and 90 kW, respectively. It achieves peak efficiency (≥94%) within a speed range from 2000 to 8000 r/min. The vehicle possesses a curb weight of 2100 kg, the wheelbase measures 2900 mm, and the front track is 1620

mm. The drag coefficient stands at 0.28, with the rolling resistance coefficient being 0.018 at a speed of 100 km/h.

Table 2. Detailed submodel parameters of the vehicle energy system

Submodel	Parameter	Value
Battery equivalent circuit	Open-circuit voltage at 50% SOC	355 V
	Internal resistance at 25°C, 50% SOC	0.05 Ω
	Internal resistance at 0°C, 50% SOC	0.12 Ω
	Internal resistance at 25°C, 20% SOC	0.08 Ω
	Polarization capacitance	5000 F
	Polarization resistance	0.01 Ω
Drive motor efficiency map	Efficiency at 2000 rpm, 50 N·m	92%
	Efficiency at 3000 rpm, 150 N·m	96%
	Efficiency at 5000 rpm, 50 N·m	94%
	Efficiency at 8000 rpm, 30 N·m	88%
	Efficiency at 1000 rpm, 100 N·m	85%
Regenerative braking system	Maximum regenerative torque	250 N·m
	Maximum regenerative power	80 kW
	Regeneration efficiency at 60 km/h, 0.2g	65%
	Regeneration efficiency at 40 km/h, 0.3g	58%
	Minimum vehicle speed for regeneration	5 km/h

The battery equivalent circuit follows a first-order RC model with parameters provided in Table 2. The drive motor efficiency values are obtained by interpolating the manufacturer-supplied efficiency map at the listed operating points. The regenerative braking system parameters are derived from the motor-inverter combined efficiency characterization.

4.1.3. Evaluation indicators

In this study, there are set evaluation indicators which are divided into three types: energy consumption performance evaluation indicators, control smoothness indicators, and real-time indicators.

(1) Control smoothness index: SOC change rate and standard deviation of motor output power.

The experiment focused on monitoring the SOC change rate of the power battery, and the calculation equation is as follows:

$$\mathrm{SOC_{rate}}=\frac{1}{N\text{-}1}\sum_{k=1}^{N\text{-}1}|\mathrm{SOC}(k\text{+}1)\text{-}\mathrm{SOC}(k)| \tag{12}$$

In equation (12), SOC(k) is the SOC of the battery at the k-th sampling time; N is the total number of sampling points throughout the process, and the measurement accuracy requirement is ±0.5%.

The standard deviation σ_p of motor output power is computed utilizing the following equation:

$$\sigma_P=\sqrt{\frac{1}{M\text{-}1}\sum_{i=1}^{M}(P_{\mathrm{motor}}(i)\text{-}\overline{P}_{\mathrm{motor}})^2} \tag{13}$$

Here, $P_{\mathrm{motor}}(i)$ signifies the motor output power at the i-th sampling point; $\overline{P}_{\mathrm{motor}}$ is the average power over the entire process; M represents the total number of power sampling points, with a sampling frequency of 100 Hz and a unit of kW.

(2) Energy consumption performance evaluation indicators: braking energy recovery rate and energy consumption per 100 kilometers.

Braking energy recovery rate can be described as the ratio of electric energy obtained throughout the braking process in comparison to the total braking energy. The calculation formula related to this is provided below:

$$E_{\mathrm{rec}}=\int_{t_{\mathrm{brake}}}P_{\mathrm{rec}}(t)\,dt\ ,\ E_{\mathrm{fric}}=\int_{t_{\mathrm{brake}}}P_{\mathrm{fric}}(t)\,dt\ ,\ \eta_{\mathrm{rec}}=\frac{E_{\mathrm{rec}}}{E_{\mathrm{rec}}+E_{\mathrm{fric}}} \tag{14}$$

In equation (14), E_{rec} is the regenerative braking energy fed back; E_{fric} is the mechanical energy consumed by friction braking, which can be estimated via the vehicle dynamics model, and the integral interval t_{brake} denotes the time interval of all braking events.

Energy consumption per 100 kilometers is:

$$E_{\mathrm{total}}=\int_0^{t_f}P_{\mathrm{draw}}(t)dt\ ,\ C_{100}=\frac{E_{\mathrm{total}}}{D}\times 100 \tag{15}$$

In equation (15), E_{total} is the total electrical energy consumed from the battery during the entire journey is (kWh). D is the total driving distance under NEDC conditions is (km); the unit is kWh/100 km.

(3) Real-time indicators: control cycle and maximum response time.

The control cycle refers to the average time required for an algorithm to accomplish one entire state perception, optimization solution, and instruction output process. The calculation equation is as follows:

$$T_{\text{avg}}=\frac{1}{K}\sum_{k=1}^{K} t_{\text{exec}}^{(k)} \quad (16)$$

In equation (16), the actual execution time of the k-th MPC iteration of $t_{\text{exec}}^{(k)}$ is in ms; K signifies the total number of control steps in the entire driving cycle; the start and end times of each optimization call are recorded using a high-precision timer.

A maximum response time is defined as the duration taken in a single execution of the algorithm under worst-case conditions, which reflects the real-time robustness of the system. It is calculated as follows:

$$T_{max}=\max_{k=1,\ldots,K}\left(t_{\text{exec}}^{(k)}\right) \quad (17)$$

In equation (17), T_{max} is used to evaluate whether the hard real-time constraint is satisfied.

Each working scenario was tested three times, with results being considered according to the arithmetic mean, so random errors are reduced.

4.2. Comparison Algorithm

This research chose three representative control strategies as a basis for comparison. These include rule-based strategies, classical MPC, and reinforcement learning algorithms. The comparisons are implemented on a unified simulation platform. The core control logic and key parameter configurations of each algorithm are depicted in Table 3.

Table 3. Introduction to comparison algorithms

Algorithm Category & Method	Core Principles & Model Formulation	Key Parameters	Control Framework & Traits
Rule- B ased [33]	Heuristic, threshold-based logic. No predictive model; reacts to the current state.	Target SOC: 60%. Upper threshold: 65%. Lower threshold: 55%. Thresholds are set based on the manufacturer's recommended operating range for the NCM811 ternary lithium battery.	Framework: Rule-based feedback control. Traits: Simple, robust, non-predictive.
Classic MPC	Uses a simplified linear battery model.	Prediction horizon N_p: 8 steps. Control horizon N_c: 2 steps. Weighting coefficients λ_1=0.6 and λ_2=0.4, calibrated via grid search over the set {0.1,0.2,…,0.9} for each coefficient on the WLTC cycle to minimize the sum of energy consumption and SOC tracking error. The linear SOC model in equation (18) is used for prediction. Constraints include motor power limits from -50 kW to 150 kW and SOC bounds from 0.2 to 0.9. Control Horizon N_c: 2 steps. Weighting coefficientsλ_1 = 0.6, λ_2 = 0.4 (calibrated via sensitivity analysis balancing energy consumption and SOC tracking across four test cycles).	Framework: MPC. Traits: Predictive but with model mismatch.
DQN [34]	Learns control policy directly from data. Observation Space: SOC, vehicle speed, required power Action Space: discretized motor power commands ranging from -50 kW to 150 kW with 21 discrete actions.	Network architecture: 3-layer FC (3-32-21), ReLU activation Training: raining: 5000 episodes on WLTC cycle with random initial SOC ∈ [30%, 80%]	Framework: DRL (Deep Reinforcement Learning) Traits: Adaptive, data-hungry, safety concerns.

		Exploration: ε-greedy with ε decay from 0.9 to 0.05 over 3000 episodes. Replay buffer: 1e5. Batch size: 64. Discount factor γ: 0.95. Learning rate: 1e-3 (Adam) Target network update: 100 steps. Reward weights: α = 0.8, β = 0.2. Training episodes: 5000 episodes on the WLTC cycle with random initial SOC uniformly distributed between 30% and 80%. Exploration: ε-greedy with ε decay from 0.9 to 0.05 over 3000 episodes. Replay buffer size: 100000. Batch size: 64. Discount factor γ: 0.95. Learning rate: 0.001 with Adam optimizer. Target network update frequency: every 100 steps. Reward weights α=0.8 and β=0.2. Convergence criterion: average reward over 100 consecutive episodes stabilizes within 2% variation.	

A constant SOC maintenance strategy is adopted as the basic comparison algorithm, with a target SOC set at 60%, and power regulation is achieved through threshold control. When the real-time SOC is higher than 65%, the system automatically increases the discharge power of the power battery to reduce the SOC; when the SOC is lower than 55%, the discharge power is reduced, and regenerative braking energy recovery is prioritized, achieving basic SOC stability through simple interval control. The benefit of the approach is low computational complexity. It does not need any complex model support, and it is suitable for a fast deployment inside embedded systems. However, that control does not provide proactive optimization for the driving conditions. The threshold values for the rule-based strategy (target SOC = 60%, upper threshold = 65%, lower threshold = 55%) are selected based on empirical calibration from the vehicle manufacturer's recommended operating range for the NCM811 ternary lithium battery.

A simplified version of MPC was chosen as the benchmark to be compared with the optimization algorithms; the linear SOC model, which neglects the temperature effects and efficiency fluctuations, was adopted:

$$SOC(t+1)= SOC(t)-\frac{(P_{bat}* \Delta t)}{(U*C)} \quad (18)$$

The meaning of the parameters in equation (18) is as follows: P_{bat} shows the battery power; Δt stands for control cycle; U denotes nominal voltage, while C represents the battery capacity. Accordingly, the prediction horizon N_p and control horizon N_c for the classic MPC are tuned through grid search over the WLTC cycle. N_p is evaluated at values of 6, 8, 10, 12, and 14 steps, with N_c fixed at 2 steps. The configuration achieving the lowest energy consumption while maintaining the control cycle within 100 ms is selected, resulting in N_p = 8 steps and N_c = 2 steps. The weighting coefficients λ_1 and λ_2 in the objective function are set to 0.6 and 0.4 respectively, following a sensitivity analysis that balances energy consumption minimization and SOC tracking accuracy across the four test cycles. This algorithm employs a prediction mechanism, and the simplified model cannot highlight non-linear characteristics of the battery under different temperatures and SOC ranges, reducing control accuracy under complicated conditions.

DQN has been employed here as a typical data-driven algorithm, creating an observation space with three state variables: current SOC, vehicle speed, and the necessary power. The action space was designed to be discretized motor power commands that range from -50 kW to 150 kW. The reward function is stated as:

$$R=-\alpha\cdot E_{total}- \beta\cdot|SOC-SOC_{ref}| \quad (19)$$

In equation (19), α =0.8 and β =0.2 are weight coefficients; E_{total} is the cumulative energy consumption; and $SOC_{ref} = 60\%$ is the target value. The network architecture employs a three-layer, fully connected neural network. There are 3 neurons located in the input layer, 32

neurons placed within a hidden layer, and 21 neurons situated at the output layer. The experience replay pool capacity is 10^5.

4.3. Performance Indicators and Results

The real-time performance metrics of all algorithms were tested on the dSPACE SCALEXIO hardware-in-the-loop platform. This platform is equipped with a multi-core processor, whose computing power is comparable to mainstream automotive domain controllers, and can realistically reflect the computational performance of the algorithms in an in-vehicle environment. Four operating scenarios give an opportunity to assess the performance during testing: the NEDC, the WLTC, actual urban commuting, and highway cruising. The control cycle was uniformly set to 100 ms, and a 100 kWh ternary lithium battery was used as the power battery model.

4.3.1. Energy consumption level indicator assessment

Fig. 5 shows the test results of energy consumption per 100 kilometers and braking energy recovery rate of the four models under four road conditions.

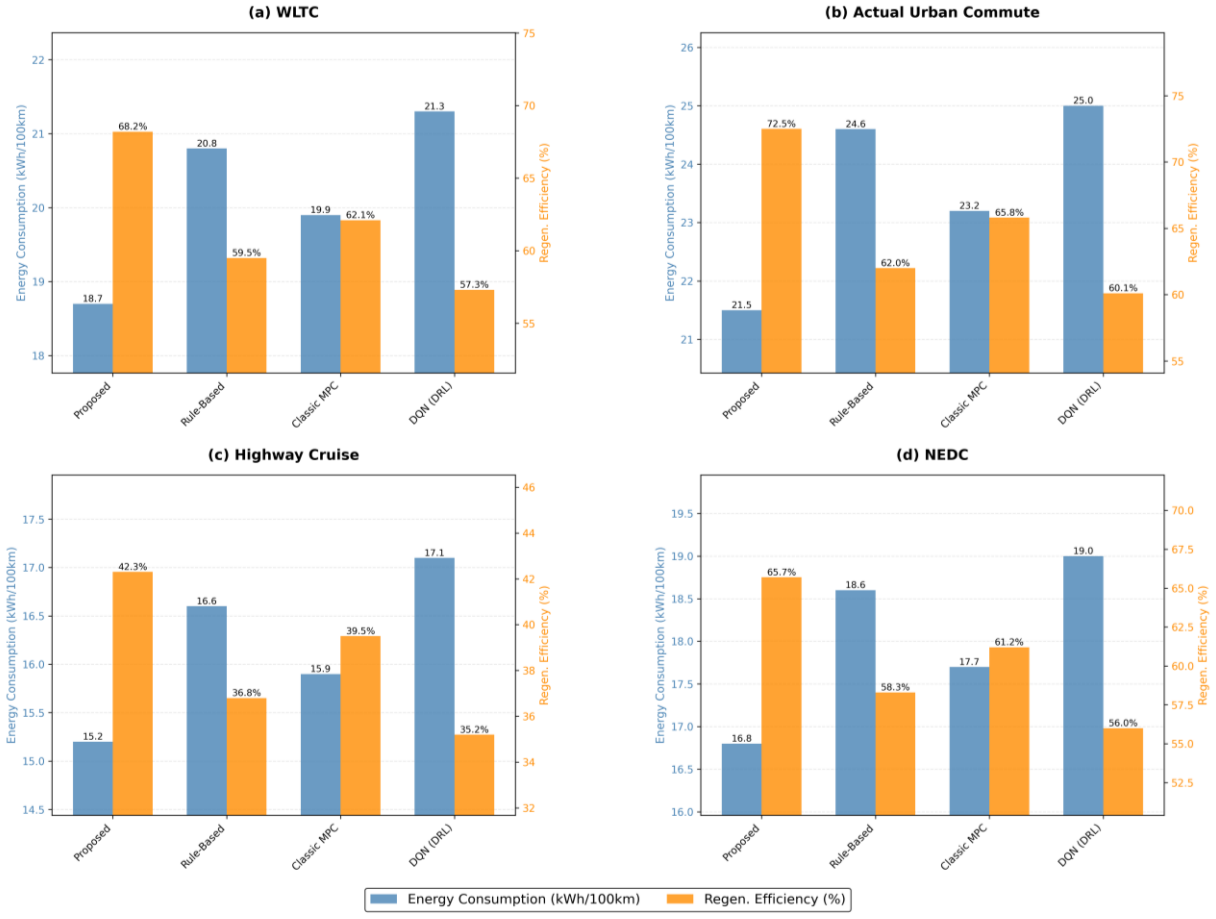

Fig. 5. Comparison of model energy consumption levels

Fig. 5(a) shows that in the WLTC combined operating condition, the energy dispatch algorithm achieves an energy consumption of 18.7 kWh/100 km, outperforming all compared algorithms. Compared to the traditional rule-based strategy (20.8 kWh/100 km), energy consumption is decreased by 10.1%; than that of the classic MPC algorithm (19.9 kWh/100 km), it is reduced by 6.0%; and compared to the deep reinforcement learning DQN method (21.3 kWh/100 km), it achieves a significant energy saving of 12.2%. The regenerative braking efficiency reached by an algorithm proposed in this research is up to 68.2%, which kind of shows that it may recover braking energy effectively in mixed dynamic conditions. This performance advantage comes from the constructed continuous-time differential equation model, which coordinates power allocation globally and gives the opportunity to maximize efficiency for using the energy.

Fig. 5(b) shows that in real urban commuting situations, the proposed algorithm obtains an energy consumption result of 21.5 kWh/100 km. This gives a major reduction by 12.6%, 7.3%, and also 14.0% as compared with the conventional strategy (24.6 kWh/100 km), classical MPC (23.2 kWh/100 km), and DQN (25.0 kWh/100 km), respectively. The regenerative braking efficiency reaches 72.5%, fully demonstrating its effective recovery capability for frequent braking kinetic energy. In urban scenarios with drastic energy flow fluctuations, the adaptability of the proposed energy scheduling algorithm is the strongest. Benefiting from the accurate modeling of nonlinear charging/discharging characteristics using differential equations, an aggressive but controllable energy scheduling strategy can be adopted by the system to ensure safety, reduce energy waste, and maintain good driving comfort.

Fig. 5(c) indicates that during steady-state high-speed cruise, the algorithm proposed herein consumes only 15.2 kWh/100 km, outperforming the regular strategy (16.6 kWh/100 km) by 8.4%, performing better than classic MPC (15.9 kWh/100 km, with a reduction of 4.4%), and significantly lower than DQN (17.1 kWh/100 km) by 11.1%. In the meantime, under this condition, the regenerative braking events rarely emerge, with a recovery efficiency of 42.3% and redundant fluctuation suppression in battery current, thus excellent energy consumption control is achieved. It can be seen that even under low-dynamic conditions, refined optimization based on differential equations still brings considerable energy efficiency benefits.

Fig. 5(d) depicted that the energy consumptions of the proposed algorithm under the NEDC standard cycle are 16.8 kWh/100 km, which is 9.7% lower compared to the regular strategy (18.6 kWh/100 km) and superior to that of classic MPC (17.7 kWh/100 km, a reduction of 5.1%) and 11.6% lower than DQN (19.0 kWh/100 km) with regenerative braking efficiency as high as 65.7%. The algorithm maintains stable and excellent performance in both standardized test cycles and real-world road scenarios, showing outstanding robustness and engineering generalization ability.

4.3.2. Controlling smoothness

Fig. 6 demonstrates the outcomes of the SOC change rate and motor power change standard deviation for the four models under four road conditions.

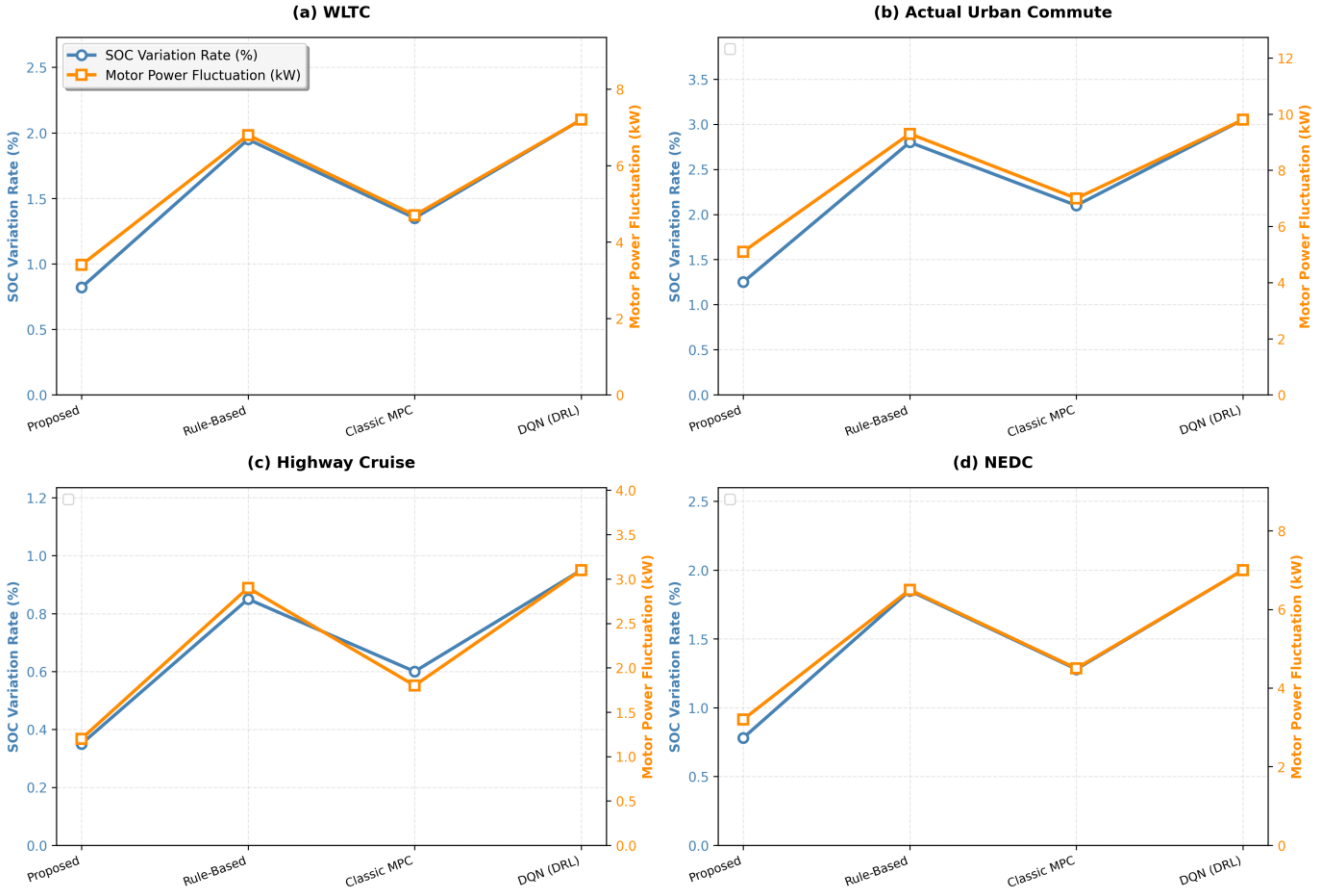

Fig. 6. Evaluation of control smoothness index

The complete WLTC test cycle shows that the algorithm in this paper exhibits a significant advantage in control smoothness. The standard deviation of power variation (σ_p = 3.4 kW) is much lower than that of other comparative algorithms, decreasing by 50% compared to the regular strategy, 27.7% compared to the classic MPC, and 52.8% compared to the DQN algorithm. The lowest SOC change rate of 0.82% indicates that the algorithm is also excellent in maintaining battery state stability. This demonstrates that the proposed control method can effectively suppress power fluctuations and provide smoother energy management under complex and variable operating conditions.

In the most challenging urban driving condition (Fig. 6(b)), facing frequent starts, stops, accelerations, and decelerations, the proposed algorithm still controls power fluctuations to 5.1 kW, which is approximately 45% and 48% lower than the regular strategy (9.3 kW) and the DQN algorithm (9.8 kW), respectively, and 27% lower than the classic MPC (7 kW). This shows that the suggested control strategy has excellent adaptability to transient conditions, effectively reduces transmission system shock, and holds considerable importance for enhancing urban driving comfort as well as the durability of components.

Under steady high-velocity cruise situations (Fig. 6(c)), fluctuations of power for every algorithm are reduced

significantly; however, the method proposed in the article continues to show a stronger smoothing property. The power standard deviation (1.2 kW) is reduced by nearly 60% compared to the rule-based strategy (2.9 kW) and the DQN algorithm (3.1 kW), and is further optimized by 33% compared to the second-best performing classic MPC (1.8 kW). At the same time, the lowest SOC change rate of 0.35% reflects the algorithm's accurate power matching capability under steady-state conditions, achieving the best balance between energy efficiency and smoothness.

Fig. 6(d) shows that in the NEDC test cycle, the power fluctuation level of the algorithm in this paper (3.2 kW) is comparable to that of the WLTC condition and is significantly better than other algorithms. It is 50.8% lower than the rule strategy and 54.3% lower than the DQN algorithm, which proves that the control strategy can maintain stable control quality in standard test cycles with different characteristics and avoid potential power oscillation problems.

4.3.3. Real-time performance indicators

The real-time performance indicators are shown in Fig. 7.

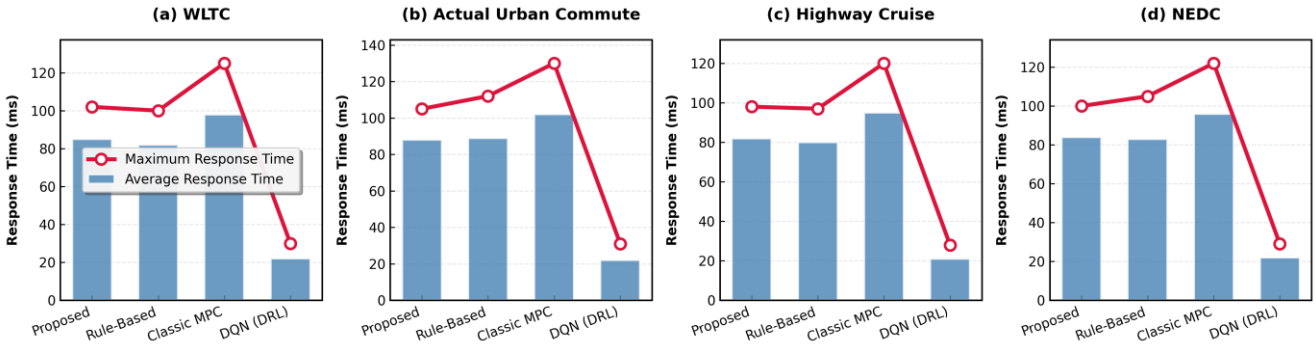

Fig. 6. Real-time performance evaluation

Fig. 7(a) shows the WLTC comprehensive operating condition. The algorithm achieves an average latency of 85ms and a maximum response time of 102ms, comparable to the regular strategy (82/100ms), while simultaneously achieving optimal energy consumption, demonstrating its ability to balance real-time performance and energy efficiency under complex and variable operating conditions. Fig. 7(b) shows the algorithm facing the challenge of high-frequency start-stop. While its average latency of 88ms and maximum response time of 105ms are a little higher than the regular strategy's 89/112ms, it far outperforms classic MPC, which has 102/130ms, thus demonstrating its robust real-time performance in highly dynamic scenarios. Fig. 7(c) gives the algorithm under high-speed cruise conditions. The mean latency is just 82 ms, and there is a maximum response time of 98 ms. It is almost as good as the lightweight regular strategy (80/97ms) and far better than classic MPC (95/120ms), verifying extreme efficiency in low-dynamic scenarios. Fig. 7(d) reflects that under the standard operating condition NEDC, the average time that this algorithm takes is 84ms, while the maximum is up to 100ms, with high consistency compared to the rule-based strategy (83/105ms). Besides, it has excellent computational stability.

For the proposed algorithm, the maximum response time reaches 105 ms in the urban commuting scenario, which exceeds the nominal 100 ms control cycle in this specific case. In such deadline miss events, the controller maintains the motor power and regenerative braking intensity at the values from the previous successful optimization step. No safety violation or instability was observed during these transient exceedances. The control system handles this occasional deadline miss by holding the previous control action unchanged until the optimization completes, ensuring system stability without safety violation.

From a computational efficiency perspective, the mean computation time of the DQN algorithm remained stable across all test conditions, standing at 21-22 ms with a maximum response time not exceeding 31 ms. This inference time corresponds exclusively to the forward pass of the trained neural network. The DQN training process is conducted offline and is not included in the real-time performance evaluation, as the trained network is deployed for inference only during online control. Combining the analysis of Figs. 5 and 6, DQN had the worst performance among all algorithms on energy consumption and control smoothness, with high energy consumption (21.3 kWh/100km) and power fluctuations (7.2 kW) under WLTC conditions. This σ_p indicates that while a purely data-driven control strategy can guarantee real-time performance in a complex dynamic environment, it is difficult to balance energy efficiency and smoothness.

The DQN algorithm's inference time of 21-22 ms per control step corresponds to the forward pass of the trained neural network. The training process itself is conducted offline and is not included in the real-time performance evaluation. All baseline algorithms were tested under identical conditions with the same vehicle model and driving cycles. Each experiment was repeated three times, and the reported results are arithmetic means. The standard deviation across runs for energy consumption was below 0.3 kWh/100 km for all algorithms, indicating statistical stability.

Meanwhile, the rule-based strategy shows similar real-time performance, ranging from 82 to 89 ms on average, with good computational stability. However, the control logic of heuristic rules σ_p is far behind the proposed algorithm in energy consumption (WLTC: 20.8 kWh/100km) and smoothness (WLTC: = 6.8 kW), which cannot adapt easily to

the dynamic requirements under diverse operating conditions. It is lightweight in computation but lacks performance.

Compared with other methods, the traditional MPC algorithm has significantly higher average computation time (95-102 ms) and maximum response time (120-130 ms). Although the energy consumption of this algorithm is lower than that of the regular strategy (WLTC: 19.9 kWh/100km), and its smoothness is also higher (WLTC: "σ_p" = 4.7 kW), it is still much lower than that of the algorithm proposed in this paper. Its maximum response time can reach 130 ms in the most dynamic urban scenario (Fig. 7(b)). In summary, though some optimizations have been achieved by the traditional MPC, its high computational complexity limits its application potential in engineering.

Under all driving conditions, the average computation time of the proposed algorithm fluctuates only within a small range of 82-88ms, showing that it is robust to changes in different driving conditions and has excellent computational efficiency, comparable to lightweight rule-based strategies. Under the WLTC comprehensive driving condition shown in Fig. 7(a), the average computation time of this algorithm is 85ms, and the maximum response time is 102ms, very close to that of the rule-based strategy (82/100ms). Overall, this algorithm realized a low energy consumption in every driving condition. It provided a good control smoothness as well, and the standard deviation of power fluctuation is more than 27% lower compared to the best algorithm. The computation time of this approach is as good as that of lightweight rule-based strategies and far below that of classic MPC. Although the algorithm is based on a complex differential equation model and includes an online optimization process, through efficient solver design, the computational cost is effectively controlled without sacrifice in real-time performance for better model accuracy, demonstrating its potential for practical deployment on automotive hardware.

All timing measurements reported in this study are obtained from the dSPACE SCALEXIO hardware-in-the-loop platform without GPU acceleration, reflecting the computational performance achievable on automotive-grade embedded hardware.

4.4. Ablation Experiment and Robustness Analysis

4.4.1. Parameter sensitivity analysis

In the continuous-time differential equation modeling framework, two important variables that affect the algorithm's accuracy and real-time performance are the discretization step size and the length of the prediction time domain. Three discretization step sizes are compared in experiments: 0.5 s, 1 s, and 2 s. In the analysis of the discretization step size, computation time based on a 0.5 s step size corresponds to the highest possible accuracy and is used as the baseline (100%), which quantifies the trade-offs between accuracy and efficiency. In the analysis of the prediction time domain, computation time is calculated at N_p=10 steps, corresponding to the energy consumption optimization inflection point, as the baseline (100%), revealing the decreasing marginal returns of lengthening the time domain of prediction. Experimental outcomes are presented in Fig. 8.

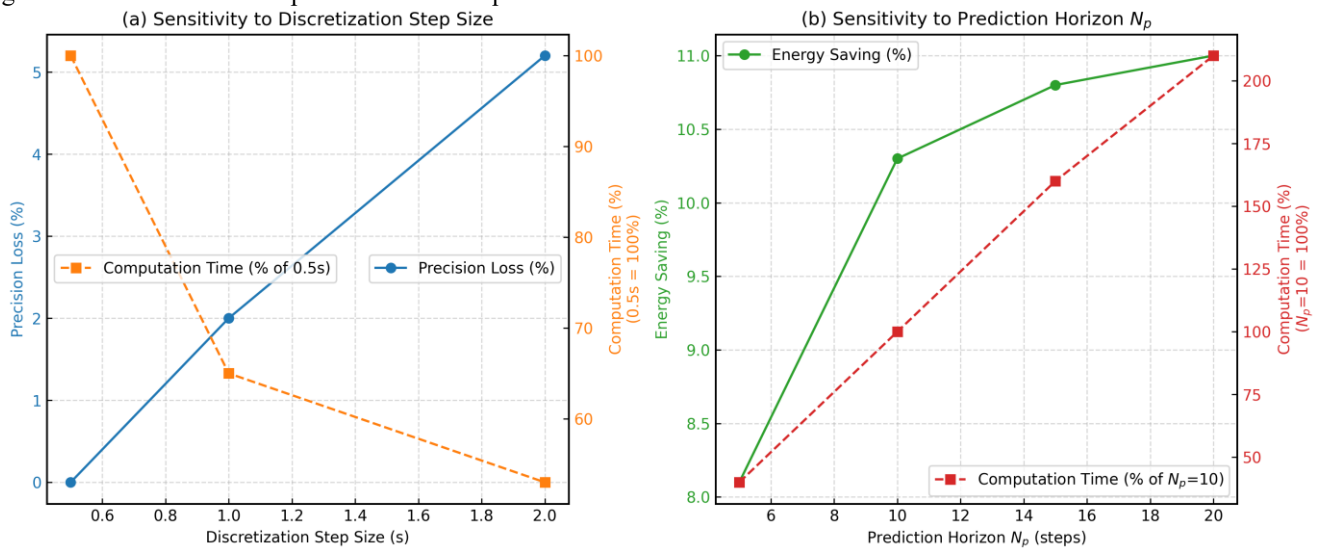

Fig. 8. Parameter sensitivity analysis

Fig. 8(a) shows that a 1-second step size represents a good compromise between accuracy and efficiency: the loss in accuracy can be maintained at 2%, and the computation time is 35% less compared to a 0.5-second step size. A larger step size of 2 seconds would require even less computational time, reducing the computation time by a further 12 % relative to the 1 -second step-size case, but the accuracy loss is above 5%, leading to a very noticeable deviation for the energy allocation strategy.

Fig. 8(b) presents the prediction time domain N_p test results. When N_p=10 steps, the energy consumption reduction rate reaches a peak of 10.3%. Continuing to increase the time domain to 15 steps, the energy consumption is reduced by only an additional 0.5%, but the calculation time increases by 60%, which shows that excessively extending the prediction time domain leads to a significant decrease in marginal benefits.

This algorithm has a great range of parameter optimizations. With a discretization step size of 1 s and a

prediction time domain of 10 steps, it can achieve a triple optimization objective: the accuracy loss is 2%, energy consumption is decreased by 10.3%, and the time consumption is reduced.

4.4.2. Analysis of ablation experiment results

In order to confirm the contribution of design elements, including the differential equation model and the SOC reference trajectory, three sets of ablation experiments are designed as follows. All the experiments were performed under WLTC conditions while keeping other parameters consistent.

The complete model is Group A, serving as the baseline when running the ablation experiments.

Group B replaced the continuous differential equations with a linear state transition model to see if it is indeed essential to use differential equations to model a highly dynamic system.

Group C removed the SOC reference trajectory constraint and only optimized energy consumption to explore the key role of active SOC management in range stability and user experience.

Group D uses a fixed regenerative braking intensity of 0.5, ignoring the dynamic coupling relationship with vehicle velocity and battery state, to verify the effect of dynamic braking distribution strategy on energy recovery efficiency.

By comparing the differences among the four groups in terms of energy consumption, SOC change rate, motor power standard deviation, and braking energy regeneration efficiency, the irreplaceability of each design element in the algorithm is identified, and the structural superiority of the complete framework is demonstrated. The ablation experiment outcomes are demonstrated in Table 4.

Table 4. Analysis of ablation experiment results

Variant	Energy Consumption (kWh/100 km)	Regenerative Braking Efficiency (%)	Motor Power Fluctuation σ_p (kW)	SOC Variation Rate (%)
A	18.7	68.2	3.4	0.82
B	19.8	60.5	4.9	1.35
C	18.2	66.1	5.2	1.78
D	19.1	52	3.6	0.85

Table 4 shows the key roles of each core component in the proposed framework, derived from the outcomes of the ablation experiments.

Compared with the complete model A, variant B (replacing the continuous-time differential equation model with a linear state transition model) suffers from serious performance degradation under WLTC conditions: it increases energy consumption by 1.1 kWh per 100 kilometers, decreases the braking energy recovery rate by 7.7%, and greatly increases motor power fluctuation (4.9 kW vs. 3.4 kW) and SOC change rate (1.35% vs. 0.82%). These prove that mechanism-based differential equation modeling is essential for accurately characterizing the nonlinear dynamics of the battery and achieving smooth and efficient energy distribution, especially under transient conditions.

When the SOC reference trajectory is removed from variant C, the algorithm has only one priority: energy minimization. Indeed, energy consumption decreases by a small margin, to 18.2 kWh/100 km, but at the price of degraded control quality: SOC change rate increases almost by two times, 1.78%, while motor power fluctuations reach as high as 5.2 kW, reflecting very aggressive, unstable battery charge and discharge behavior. In this way, it has been shown that, in the absence of an explicit SOC management mechanism, the system would sacrifice driving smoothness and battery health for minor gains in energy efficiency. Therefore, the SOC reference trajectory is indispensable in practical engineering applications.

A fixed regenerative braking intensity of 0.5 (variant D) did not significantly affect SOC stability, but the braking energy recovery rate decreased sharply by 16.2% (52.0% vs. 68.2%), and the energy consumption per 100 kilometers also increased by 0.4 kWh accordingly. This shows that, when compared with static rules, a regenerative braking strategy that relies on real-time dynamic adjustments under operating conditions has an important role in maximizing kinetic energy recovery efficiency.

The ablation experiment verified that the complete model, by integrating continuous dynamic modeling, active SOC management, and adaptive braking control, achieved synergistic optimization of energy efficiency, stability, and energy recovery capability, and that each component is indispensable.

4.4.3. Robustness verification under extreme operating conditions

Using SOC=80% as the baseline, tests were conducted on two typical disturbance factors: low battery SOC and driving style. The test findings are depicted in Table 5.

Table 5. Robustness verification

Perturbation Scenario	Test Condition	Proposed-Energy Consumption (kWh/100 km)	Rule-Based-Energy Consumption (kWh/100 km)
Baseline SOC	SOC = 80 %	18.7	20.1
Low SOC	SOC = 30%	19.3	20.7
Aggressive Driving	40% increase in rapid acceleration/deceleration	19.22	twenty-one

Table 5 shows the robustness experimental verification. In the low-battery scenario of SOC=30%, the battery charging and discharging efficiency decreases, and the algorithm's energy consumption increases by 3.2% compared to SOC=80%, but is still 6.8% lower than the traditional rule-based strategy. In the face of aggressive driving styles-a 40% increase in the frequency of rapid acceleration/deceleration-the algorithm's energy consumption is decreased by 8.5% compared to the rule-based strategy, which verifies the algorithm's strong adaptability to fluctuations in driving behavior. This robustness comes from an accurate description of the nonlinear characteristics of the battery through a differential equation model and the capability of the rolling optimization mechanism to correct in real-time for disturbances.

It can achieve effective energy allocation with the assurance of real-time computation by rationally configuring the discretization parameters and prediction time domain. Besides, it maintains stable energy-saving effects under low SOC and extreme driving behaviors, and has potential for practical vehicle application.

5. Conclusion

This research constructs an energy dispatch algorithm for battery electric vehicles that integrates continuous-time differential equation modeling and model predictive control. The research results fully verify that the technical path of "continuous-time differential equation modeling" effectively overcomes the long-standing "accuracy-efficiency-safety" triangle bottleneck in the domain of new energy vehicle energy management. Regarding particular technical use, by establishing a coupled differential equations model which includes the battery SOC dynamics, vehicle movements, and regenerative braking mechanism, the physical consistency in the system description is being enhanced significantly. Combined with implicit Euler discretization and efficient numerical solution strategies, an average control cycle of 85 ms and a maximum of 102 ms are achieved under WLTC conditions, meeting the 100 ms real-time requirements of the vehicle system. Under four typical operating conditions—WLTC, NEDC, actual urban commuting, and highway cruising—the algorithm's energy consumption per 100 km is stable in the range of 15.2-21.5 kWh/100 km, which is better than the classic MPC and DQN methods. The energy recovery rate from braking ranges from 42.3% to 72.5%, while the SOC changing rate varies from 0.35% to 1.25%. It creates a balance among energy efficiency, driving stability, and the health of batteries. Ablation experiments further verified that performance improvement is underpinned by differential equation modeling, SOC reference trajectory, and dynamic regenerative braking strategy. The algorithm demonstrates robust, comprehensive performance against complex transient and steady-state conditions, which finally confirms the effectiveness and superiority of the method in achieving synergistic optimization across the three objectives of "accuracy-efficiency-safety." This research provides a theoretically rigorous and engineeringly deployable technical path for intelligent electric vehicle energy management, V2G scheduling, and personalized energy-saving driving, possessing potential for practical vehicle application.4

Acknowledgement

N/A

Authorship Contribution Statement

Xue Li: Writing-Original draft preparation, Conceptualization, Supervision, Project administration.

Conflicts of Interest

The authors declare that there is no conflict of interest regarding the publication of this paper.

References

[1] S. Qin, Y. Xiong, and X. Wang, “Can non-subsidised policies for new energy vehicles improve the quality of enterprise innovation? evidence from China,” Asian Journal of Technology Innovation, vol. 33, no. 2, pp. 655-687, 2025.

[2] Z. Yang, H. Huang, and F. Lin, “Sustainable electric vehicle batteries for a sustainable world: perspectives on battery cathodes, environment, supply chain, manufacturing, life cycle, and policy,” Advanced Energy Materials, vol. 12, no. 26, p. 2200383, 2022.

[3] W. Zhao and B. Luethje, “Disintegration, core competency, and industry structure: Chinese automotive OEMs in electrification and digitalisation,” International Journal of Automotive Technology and Management, vol. 25, no. 2, pp. 148-166, 2025.

[4] Y. Yi, Z. Y. Sun, B.-A. Fu, W.-Y. Tong, and R.-S. Huang, “Accelerating towards sustainability: policy and technology dynamic assessments in China’s road transport sector,” Sustainability, vol. 17, no. 8, p. 3668, 2025.

[5] M.S.H. Lipu, A.A. Mamun, S. Ansari, M.S. Miah, K. Hasan, S.T. Meraj, M.G.M. Abdolrasol, T. Rahman, "Battery management, key technologies, methods, issues, and future trends of electric vehicles: a pathway toward achieving sustainable development goals," Batteries, vol. 8, no. 9, p. 119, 2022.

[6] H. E. Ghadbane, S. Barkat, A. Houari, S. Ferahtia, A. Djerioui, and T. Mesbahi, "A new energy management strategy for electric vehicles based on optimal adaptive state machine control," Smart Grids and Sustainable Energy, vol. 9, no. 2, p. 28, 2024.

[7] B. Huang, W. Yu, M. Ma, X. Wei, and G. Wang, "Artificial-intelligence-based energy management strategies for hybrid electric vehicles: a comprehensive review," Energies, vol. 18, no. 14, p. 3600, 2025.

[8] P. Pillai, S. Sundaresan, P. Kumar, K. R. Pattipati, and B. Balasingam, "Open-circuit voltage models for battery management systems: a review," Energies, vol. 15, no. 18, p. 6803, 2022.

[9] S. Liu, Z. Li, H. Ji, L. Wang, and Z. Hou, "A novel anti-saturation model-free adaptive control algorithm and its application in the electric vehicle braking energy recovery system," Symmetry, vol. 14, no. 3, p. 580, 2022.

[10] A. Recalde, R. Cajo, W. Velasquez, and M. S. Alvarez-Alvarado, "Machine learning and optimization in energy management systems for plug-in hybrid electric vehicles: a comprehensive review," Energies, vol. 17, no. 13, p. 3059, 2024.

[11] L. Zhu, F. Tao, Z. Fu, M. Li, and G. Deng, "Safety-involved co-optimization of speed trajectory and energy management for fuel cell-battery electric vehicle in car-following scenarios," Complex & Intelligent Systems, vol. 11, no. 1, p. 89, 2025.

[12] A. R. Singh, R. S. Kumar, M. Bajaj, C. B. Khadse, and I. Zaitsev, "Machine learning-based energy management and power forecasting in grid-connected microgrids with multiple distributed energy sources," Scientific Reports, vol. 14, no. 1, p. 19207, 2024.

[13] X. Guo, X. Zhang, J. Dong, and X. Yang, "Optimal allocation of urban new energy vehicles and traditional energy vehicles considering pollution and cost," Environment, Development and Sustainability, vol. 26, no. 3, pp. 6007-6026, 2024.

[14] J. Uralde, O. Barambones, A. del Rio, I. Calvo, and E. Artetxe, "Rule-based operation mode control strategy for the energy management of a fuel cell electric vehicle," Batteries, vol. 10, no. 6, p. 214, 2024.

[15] J. Zhuang, P. Li, L. Liu, H. Ma, and X. Cheng, "Energy management strategy for hybrid electric vehicles based on experience-pool-optimized deep reinforcement learning," Applied Sciences, vol. 15, no. 17, p. 9302, 2025.

[16] Q. Zhang and X. Fu, "A neural network fuzzy energy management strategy for hybrid electric vehicles based on driving cycle recognition," Applied Sciences, vol. 10, no. 2, p. 696, 2020.

[17] E. Türker, E. Bulut, A. Kahraman, M. Çakıcı, and F. Öztürk, "Estimation of energy management strategy using neural-network-based surrogate model for range extended vehicle," Applied Sciences, vol. 12, no. 24, p. 12935, 2022.

[18] C. Du, S. Huang, Y. Jiang, D. Wu, and Y. Li, "Optimization of energy management strategy for fuel cell hybrid electric vehicles based on dynamic programming," Energies, vol. 15, no. 12, p. 4325, 2022.

[19] R. Schmid, J. Buerger, and N. Bajcinca, "Energy management strategy for plug-in-hybrid electric vehicles based on predictive PMP," IEEE Transactions on Control Systems Technology, vol. 29, no. 6, pp. 2548-2560, 2021.

[20] B. Zhao, R. Liu, D. Shi, S. Li, Q. Cai, and W. Shen, "Optimal control strategy of path tracking and braking energy recovery for new energy vehicles," Processes, vol. 10, no. 7, p. 1292, 2022.

[21] H.-B. Yuan, W.-J. Zou, S. Jung, and Y.-B. Kim, "Optimized rule-based energy management for a polymer electrolyte membrane fuel cell/battery hybrid power system using a genetic algorithm," International Journal of Hydrogen Energy, vol. 47, no. 12, pp. 7932-7948, 2022.

[22] S. Singh, S. N. Singh, and A. N. Tiwari, "PMSM drives and its application: an overview," Recent Advances in Electrical & Electronic Engineering, vol. 16, no. 1, pp. 4-16, 2023.

[23] Y. Ji, J. Zhang, C. He, X. Hou, W. Liu, and J. Han, "Wheel braking pressure control based on central booster electrohydraulic brake-by-wire system," IEEE Transactions on Transportation Electrification, vol. 9, no. 1, pp. 222-235, 2022.

[24] X. Zhang, J. Hou, Z. Wang, and Y. Jiang, "Study of SOC estimation by the ampere-hour integral method with capacity correction based on LSTM," Batteries, vol. 8, no. 10, p. 170, 2022.

[25] Z. Qin, L. Chen, M. Hu, and X. Chen, "A lateral and longitudinal dynamics control framework of autonomous vehicles based on multi-parameter joint estimation," IEEE Transactions on Vehicular Technology, vol. 71, no. 6, pp. 5837-5852, 2022.

[26] C. Li, G. Zhuo, C. Tang, L. Xiong, W. Tian, L. Qiao, "A review of electro-mechanical brake (EMB) system: structure, control and application," Sustainability, vol. 15, no. 5, p. 4514, 2023.

[27] N. T. Anh, C.-K. Chen, and X. Liu, "An efficient regenerative braking system for electric vehicles based on a fuzzy control strategy," Vehicles, vol. 6, no. 3, pp. 1496-1512, 2024.

[28] J. Xiao, Q. Li, Y. Bi, M. Cai, B. Dunn, T. Glossmann, J. Liu, T. Osaka, R. Sugiura, B. Wu, J. Yang,

"Understanding and applying coulombic efficiency in lithium metal batteries," Nature Energy, vol. 5, no. 8, pp. 561-568, 2020.

[29] D. Salazar and M. Garcia, "Estimation and comparison of SOC in batteries used in electromobility using the Thevenin model and Coulomb ampere counting," Energies, vol. 15, no. 19, p. 7204, 2022.

[30] Y. Wang, C. Li, Q. Sun, and Y. Chang, "Research on SOC estimation of lithium-ion batteries based on robust full order proportional integral observer," International Journal of Electrochemical Science, vol. 19, no. 8, p. 100645, 2024.

[31] M. Aida, "Fourth-order Runge-Kutta method for solving applications of system of first-order ordinary differential equations," Enhanced Knowledge in Sciences and Technology, vol. 2, no. 1, pp. 517-526, 2022.

[32] X. Xiong, Y. Bai, R. Shi, S. Kamal, Y. Wang, and Y. Lou, "Discrete-time twisting algorithm implementation with implicit-Euler ZOH discretization method," IEEE Transactions on Circuits and Systems II: Express Briefs, vol. 69, no. 8, pp. 3435-3439, 2022.

[33] N.-A. Nguyen, P.-H. La, and S.-J. Choi, "Novel high-speed state-of-charge alignment algorithm for EV battery maintenance," IEEE Transactions on Industrial Electronics, vol. 71, no. 12, pp. 15724-15733, 2024.

[34] K. Chang, D. Chen, Z. Chen, T. Yin, S. Hu, X. Xu, P. Pei, "Novel energy management strategy for fuel cell hybrid vehicles considering power following based on improved deep Q-network," Automotive Innovation, vol. 8, no. 4, pp. 1031-1046, 2025.